

Understanding the intrinsic mechanism of the giant magnetostriction in binary and alloyed FeGa solid solutions

Jiejue Niu,¹ Keyu Yan,¹ Yichen Xu,¹ Yuye Wu^{1,*}, Enke Liu,² Zhongheng Fu,³ Jiheng Li,⁴ Xuexu Gao,⁴ Xing Mu,⁵ Bingjie Liu,⁵ Xiaoxiao Wang,¹ Yunquan Li,¹ Jingmin Wang,¹ and Chengbao Jiang^{1,†}


¹*School of Materials Science and Engineering, Beihang University, Beijing 100191, People's Republic of China*

²*State Key Laboratory for Magnetism, Institute of Physics, Chinese Academy of Sciences, Beijing 100190, People's Republic of China*

³*Beijing Advanced Innovation Center for Materials Genome Engineering, Institute for Advanced Materials and Technology, University of Science and Technology Beijing, Beijing 100083, People's Republic of China*

⁴*State Key Laboratory for Advanced Metals and Materials, University of Science and Technology Beijing, Beijing 100083, People's Republic of China*

⁵*Department of Functional Material Research, Central Iron and Steel Research Institute, Beijing 100081, People's Republic of China*

 (Received 7 August 2023; revised 1 December 2023; accepted 3 January 2024; published 22 January 2024)

Doping nonmagnetic Ga atoms into Fe leads to the enhancement in magnetostriction by ~ 10 times in the FeGa solid solutions; the fundamental mechanism of the anomalous enhancement has attracted substantial attention. However, current experimental methods are difficult to reveal the origin because of their inability in the electronic and atomic scales. In this work, we utilized first-principles calculations to unveil the origin of giant magnetostriction in FeGa solid solutions. Ga doping results in the random substitution of Fe by Ga in the disordered $A2$ matrix and the formation of $L6_0$ nanoheterogeneities simultaneously. The former weakens the strength of Fe–Fe metallic bonding framework, thus leading to the lattice softening as presented by the sharp reduction in elastic constant c' [$c' = (c_{11} - c_{12})/2$]. The latter strengthens the magnetoelastic coupling effect by regulating the density of states of $3d$ orbits of Fe atoms inside and adjacent to the nanoheterogeneities, resulting in the 3 times larger magnetoelastic coupling coefficient $-b_1$. The two effects synergistically offer the giant magnetostriction in FeGa solid solutions based on the relationship of $\lambda_{001} = -(b_1/3c')$. Furthermore, the influence of elemental doping, including Co, Ni, P, and Tb, on magnetostriction is systematically studied. It is demonstrated that Tb is the sole alloying element which can enhance the magnetoelastic coupling effect strongly, allowing FeGa-Tb supercell to present an ultrahigh magnetostriction of 738 ppm, which is over 2 times larger than that of the FeGa supercells. This work offers insights into the origin of giant heterogeneous magnetostriction in Fe-based solid solutions, which benefits the development of high-performance FeGa-based magnetostrictive materials.

DOI: [10.1103/PhysRevB.109.014417](https://doi.org/10.1103/PhysRevB.109.014417)

I. INTRODUCTION

Magnetostriction effect is the linear strain output under the application or removal of external magnetic field [1,2]. Materials with giant magnetostriction can be applied as converters of electromagnetic energy into mechanical energy or vice versa, rendering them to play crucial roles in deep-water sonar [3,4], high-precision machining [5–9], ultrasonic devices [10,11], etc. Since the observation of magnetostriction effect in pure nickel by Joule in 1842, the first-generation magnetostrictive materials of Fe, Ni as well as Fe-Ni alloys were developed soon afterwards, and they were utilized as sonar materials in underwater vehicles in the 1910s [2]. However, their saturation magnetostrictions fail to surpass 70 ppm. With the continuous discovery of substantial rare-earth based functional materials, the second-generation magnetostrictive materials of $Tb_{0.3}Dy_{0.7}Fe_{1.92}$ alloy with face-centered-cubic Laves phase (commercially known as Terfenol-D) were developed in 1975 [12]. Giant magnetostriction of over 1000

ppm can be achieved on account of the strong spin-orbit coupling between Tb/Dy and Fe, making them the preferential choice for sonar energy conversion materials [13–17]. The drawback is, the mass fraction of heavy rare-earth Tb and Dy exceeds 60 wt. %; the massive usage of Terfenol-D may give rise to serious challenges in heavy rare-earth resource and material cost [18]. Moreover, the fundamental brittleness of the $Tb_{0.3}Dy_{0.7}Fe_{1.92}$ intermetallic causes great difficulties in materials processing and high cracking risk during high-frequency vibration. Therefore, novel cost-effective magnetostrictive materials with excellent combination properties are eagerly demanded towards the extensive application in the aforementioned critical areas.

Recently, a series of Fe-based solid solutions (e.g., FeGa, Fe-Al, Fe-Si, Fe-Ge, etc.) [19–29], as represented by FeGa, were observed to have significantly superior magnetostriction compared with pure Fe. The highest magnetostriction exceeds ~ 300 ppm in FeGa single crystals; the magnitude is 10 times higher than that of pure Fe [30,31]. The solid solutions also present good ductility and lower cost. These advantages are of great significance to promote the applications. More interestingly, the design concept of the Fe-based solid solutions

*Corresponding authors: wuyuye@buaa.edu.cn

†Corresponding authors: jiangcb@buaa.edu.cn

(e.g., FeGa) is a disruptive innovation in comparison to the conventional magnetostrictive materials (e.g., Fe, Ni, FeNi, and Terfenol-D), as embodied in the following three aspects. First, conventional magnetostrictive materials are designed based on single or combination of ferromagnetic elements. Instead, doping nonmagnetic atoms (Ga, Al, Si, Ge, Mo, etc.) can strengthen magnetostriction without changing the disordered body-centered-cubic (bcc) structure (A2 structure) in the matrix phase [32,33]. Second, giant magnetostriction requires a relatively “soft” lattice in general, which renders a larger output strain during the transition from magnetic energy to elastic energy. The dissolved atoms are normally considered to induce solid-solution hardening, which is harmful to magnetostriction. However, an opposite effect is inexplicably detected in these Fe-based solid solutions [34–37]. Third, a proper concentration of Ga solute (10–27 at. %) leads to the existence of local chemical ordering nanoheterogeneities in the FeGa alloys, generating the nanoscale heterogeneous microstructures which are noteworthy different from the homogeneous microstructures in conventional magnetostrictive materials (e.g., Fe, Ni, Tb-Dy-Fe). Similar microstructure of nanoheterogeneities was also discovered in other Fe-based solid solutions. Accompanying with the formation of nanoheterogeneities, the magnetostriction is further reinforced [20,21,38–42]. Therefore, the nanoheterogeneities are interpreted as a main origin of magnetostriction enhancement. These effects may indicate magnetostriction mechanisms in Fe-based solid solutions, which is promising to open an avenue for a substantial development in magnetostrictive materials.

Investigating the magnetostriction mechanism in Fe-based solid solutions remains a challenge. The matrix is disordered bcc phase with random atomic configurations [33]; it is almost impossible to accurately depict the lattice structure, as demonstrated by previous transmission electron microscope investigations and x-ray characterizations. Meanwhile, the interaction between the nanoheterogeneities and the matrix is hard to reveal using experimental methods. Here, we use the mature special quasirandom-structure (SQS) method to treat the disordered supercells [43,44], which is already extensively applied in various material systems with disordered structures, e.g., high-/medium-entropy alloys, disordered solid solutions, etc. [45–47]. Furthermore, the structure of local chemical ordered nanoheterogeneities can also be inserted into the disordered supercell artificially in terms of the magnetostriction mechanism, considering that magnetostriction is dominated by two key factors, elastic constants (c') and magnetoelastic coupling coefficient (b_1), according to formula (1) [48]:

$$\lambda_{001} = -\frac{b_1}{3c'}. \quad (1)$$

The elastic constant c' is expressed by $c' = \frac{c_{11}-c_{12}}{2}$. The magnetoelastic coupling coefficient b_1 can be deemed as the response of change in magnetic anisotropy (MA) energy to the lattice distortion strain, as reported by Wu *et al.* [49,50]. The MA energy originates from spin-orbit coupling (SOC); the tiny lattice distortion (corresponds to magnetostriction) can be treated as a perturbation to SOC [51,52]. Thus, the magnetoelastic coupling is understood as the coupling between SOC and lattice distortion, which can be revealed by

analyzing the d states of electrons of Fe atoms near the Fermi level [53–57]. Therefore, combining SQS method and first-principles calculations based on density-functional theory (DFT) is the most promising solution to unveil the origin of giant magnetostriction in the Fe-based solid solutions.

In this work, we carried out a systematic first-principles calculations on the origin of magnetostriction enhancement in FeGa alloys. Several supercells including pure Fe and FeGa alloy with A2 structure, FeGa supercell with locally ordered structure inserted, were established using SQS method. The influence of Ga alloying on magnetostriction was analyzed. The synergetic effects of lattice softening caused by Ga solid solution and enhancement in magnetoelastic coupling induced by the ordered nanoheterogeneities were observed, which are deemed to be responsible for the giant magnetostriction in FeGa alloys. Furthermore, the evolutions in magnetostriction induced by different alloying elements including $3d$ transition elements of Ni and Co, main-group element of P, and rare-earth element of Tb, were contrastively investigated. This work reveals the fundamental origin of surprising giant magnetostriction in FeGa-based solid solutions, and offers the guidance for designing high-performance materials.

II. METHOD

A. Establishment of supercells

The supercell of pure Fe is a typical A2 bcc lattice comprised of 2 Fe atoms. In terms of FeGa alloys, the A2 and $L6_0$ -inserted supercells are generated by the Alloy Theoretic Automated Toolkit (ATAT) software [58] using SQS method. The FeGa-A2 supercells were established with $2 \times 2 \times 2$ dimensions, which consist of 13 Fe atoms and 3 Ga atoms (corresponding to nominal composition of $\text{Fe}_{81.25}\text{Ga}_{18.75}$). For identifying the repeatability, nine different supercells were calculated. Their elastic constants show high consistence, indicating that these FeGa-A2 supercells should possess similarity in elastic properties and correlated physical properties. Therefore, we selected one of them for further investigation. Regarding the $L6_0$ -inserted supercells, 60 larger $4 \times 4 \times 4$ cells which contain 104 Fe atoms and 24 Ga atoms (corresponding to nominal composition of $\text{Fe}_{81.25}\text{Ga}_{18.75}$) were established by SQS method. Among the four supercells, two of them have one $L6_0$ structure inside, the other two have two $L6_0$ structures inside. For each group, we calculated the total energy of each supercell, and selected the lower-energy one for further investigation. Then, these extracted supercells were further studied. The lattice constants of each supercells were set based on previous references [21,31]. During the investigation, an additional bcc supercell containing 127 Fe and only 1 Ga was built to reveal the influence of Ga on bonding framework.

B. Calculation and analysis of magnetostriction

The first-principles calculations were executed employing the Vienna *Ab initio* Simulation Package (VASP) [59]. The projector augmented-wave methodology [60] was applied in conjunction with the Perdew, Burke, and Ernzerhof exchange-correlation functional [61]. The plane-wave cut-off energy was established at a threshold of 500 eV. The

computational framework involved the use of a Γ -centered $5 \times 5 \times 5$ Monkhorst-Pack k -point mesh, accompanied by an energy convergence of 10^{-6} eV per cell and a force convergence of 10^{-3} eV/Å. We also checked different criteria for energy convergence and force convergence, and demonstrated that further tightening the energy convergence and force convergence has negligible effect on the calculation results. The anisotropic magnetostriction coefficient λ_{001} quantifies the proportional alteration in length along the [001] direction, indicative of tetrahedral distortion, when a previously demagnetized substance is subjected to magnetization. Linear magnetostriction in FeGa from zero to saturated magnetic field has been proven to be volume-consistent distortions. The coefficients of anisotropic magnetostriction under volume-consistent distortions were computed using formula (2) [62,63]:

$$\lambda_{001} = -\frac{2dE_{MA}/d\varepsilon}{3d^2E_{rel}/d\varepsilon^2}, \quad (2)$$

where E_{MA} and E_{rel} represent, respectively, the MA energy and relative energy change of the supercell and ε is the strain of lattice distortion. Combining with formula (1), it is deduced that the relationship between b_1 and E_{MA} is $b_1 = -\frac{2}{3V_0} \frac{dE_{MA}}{d\varepsilon}$, and the relationship between c' and E_{rel} is $c' = \frac{1}{3V_0} \frac{d^2E_{rel}}{d\varepsilon^2}$. The calculation of elastic constants, encompassing c_{11} , c_{12} , and c_{44} , can be successfully accomplished utilizing the AELAS code, under the theoretical framework of the energy-strain correlation [64]. E_{MA} delineates the energy differential between structures with identical atomic arrangements but divergent spin orientations. In the context of tetragonal magnetostriction $E_{MA} = E_{100} - E_{001}$, with the upper indices in the right parts of the equations symbolizing the spin directions. During the calculation of E_{MA} , we set the criteria of energy convergence ranging from 10^{-7} to 10^{-11} eV per cell, and found that the calculation results of E_{MA} were basically unchanged with the energy convergence lower than 10^{-9} eV per cell; therefore, we selected 10^{-9} eV per cell as the energy convergence for the magnetostriction calculation.

Spin-orbit coupling (SOC) is a pivotal interaction that significantly influences the formation of E_{MA} . It is imperative to underscore that SOC is the fundamental factor for E_{MA} , with its lowest-order contribution to total energy being of particular interest [65,66].

$$E^{SOC} = -\xi^2 \sum_{o,u} \frac{|\langle o|\hat{\sigma} \cdot \hat{L}|u\rangle|^2}{\epsilon_u - \epsilon_o}, \quad (3)$$

where o and u represent the occupied and unoccupied states, respectively.

Further analyses including density of states and charge-density difference were evaluated through the output of the VASPKIT [67].

III. RESULTS AND DISCUSSION

A. Calculation of magnetostriction of Fe and FeGa supercells

The precondition of using DFT to investigate the magnetostriction is the establishment of the supercells, in which every site should be occupied by a certain atom. The supercells which are mainly studied in this work are displayed in

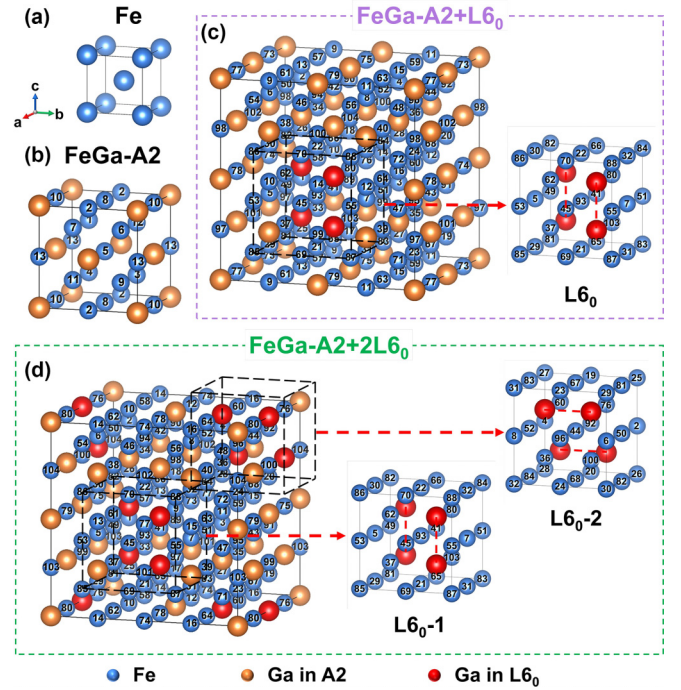


FIG. 1. Supercells utilized for investigation: (a) pure Fe; (b) FeGa-A2; (c) FeGa-A2 + $L6_0$; and (d) FeGa-A2 + $2L6_0$. Supercells in (b)–(d) are generated using SQS method. The locally ordered structure in (c), (d) is extracted for illustration.

Fig. 1. Pure Fe has a simple bcc structure with one Fe at the corner and one at body center, as shown in Fig. 1(a). The FeGa-A2 supercell, which contains $2 \times 2 \times 2$ A2 unit cells, is generated by SQS method, in order to simulate the disorder situation with random atomic configurations, as typically shown in Fig. 1(b). The composition of $Fe_{13}Ga_3$ ($Fe_{81.25}Ga_{18.75}$) is very close to the ideal composition of $Fe_{81}Ga_{19}$, which has the optimal magnetostriction. For investigating the function of nanoheterogeneity structure, we inserted its structure into a larger cell with $4 \times 4 \times 4$ A2 unit cells ($Fe_{104}Ga_{24}$, corresponding to the nominal composition of $Fe_{81.25}Ga_{18.75}$). As previously reported, the nanoheterogeneity has a face-centered-tetragonal $L6_0$ structure [23,30]. For a better match with bcc-A2 matrix, the $L6_0$ structure can be treated as a body-centered-tetragonal (bct) structure for convenience. In this case, the features of the bct- $L6_0$ structure are the nonadjacent Ga-Ga atomic pairs along $[001]_{bct}$ directions. Substantial $4 \times 4 \times 4$ FeGa supercells are generated using SQS method; among them, two supercells are extracted by the criterion that bct $L6_0$ structure exists inside, as indicated in Figs. 1(c) and 1(d). Only one bct $L6_0$ structure is detected in the former supercell (namely A2 + $L6_0$), and two bct $L6_0$ structures which are perpendicular to each other can be observed in the latter one (namely A2 + $2L6_0$). In the following, the origin of giant magnetostriction in FeGa solid solutions is revealed using the established supercells. Here it is worth emphasizing that periodic boundary conditions which may influence the results are also considered during the calculation. We studied the influence of different sizes of supercells ($2 \times 2 \times 2$, $3 \times 3 \times 3$, and $4 \times 4 \times 4$) on the calculation results of elastic constants. It is demonstrated that

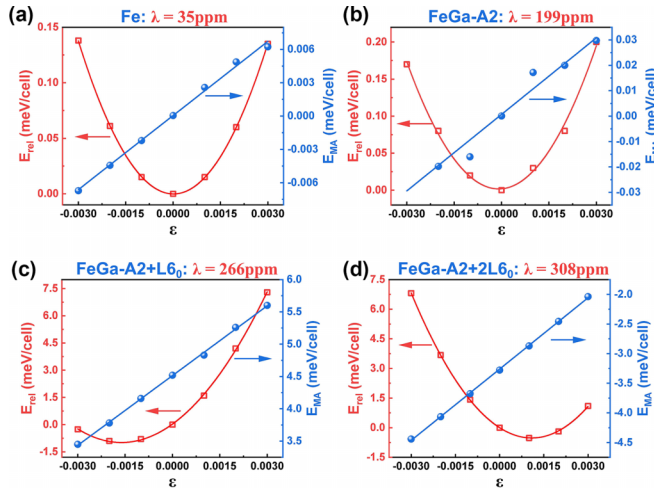


FIG. 2. Calculation of magnetostriction by fittings of relative energy change (E_{rel}) and magnetic anisotropic energy (E_{MA}) vs the lattice distortion strain (ϵ) for the established supercells: (a) pure Fe; (b) FeGa-A2; (c) FeGa-A2 + $L6_0$; and (d) FeGa-A2 + $2L6_0$.

the calculated elastic constants of different sizes of supercells are less different and consistent. Therefore, we considered that the interaction has negligible effect on the calculation results. The supercell used in the text should be reasonable to rule out artificial interaction between the repeated images of the same supercell within the applied periodic boundary conditions.

Magnetostriction (λ_{001}) of the four cells is calculated through a quadratic fitting of relative energy change (E_{rel}) and linear fitting of magnetoanisotropic energy (E_{MA}) versus the lattice distortion strain (ϵ), as presented in Fig. 2. The profiles of the curves exhibit a high degree of fitting, demonstrating the high quality of our theoretical data. The magnetostriction of the four cells is calculated to be 35, 199, 266, and 308 ppm, respectively. Overall, FeGa supercells exhibit significantly superior magnetostriction than pure Fe, and the introduction of $L6_0$ structure produces further enhancement in magnetostriction. Especially, the magnitudes of magnetostriction of pure Fe and $L6_0$ -inserted FeGa supercells are in good agreement with experimentally measured values in corresponding single crystals [2], indicating the reliability of the calculation method.

B. Mechanism of enhancement in magnetostriction by Ga doping in FeGa alloys

We next attempt to split the contribution of Ga solid solution and $L6_0$ structure to magnetostriction, respectively. Figure 3(a) summarizes the computed elastic constants, including c_{11} , c_{12} , c_{44} , and c' , of the four supercells, for revealing the evolution in elastic properties with the variation in composition and lattice structure. The comparison between Fe and FeGa-A2 supercells indicates that neither c_{12} nor c_{44} shows remarkable difference in values, whereas the value of c_{11} exhibits a sharp reduction from 247.8 GPa in Fe to 180.3 GPa in FeGa-A2 supercell with the random solid solution of Ga, which is responsible for the decrease in c' . Among the three FeGa supercells, slight deviation is discovered in all the

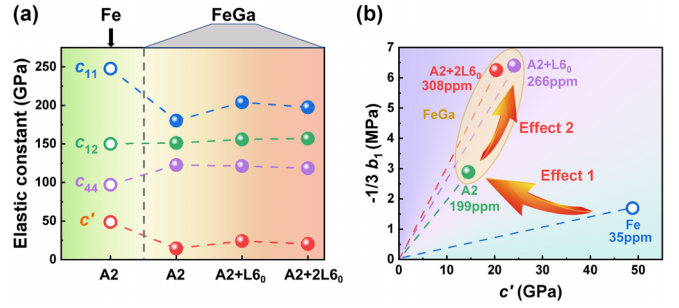


FIG. 3. (a) Direct comparison of elastic constants including c_{11} , c_{12} , c_{44} , and c' , among the four supercells: pure Fe, FeGa-A2, FeGa-A2 + $L6_0$, and FeGa-A2 + $2L6_0$. (b) The function of $-\frac{1}{3}b_1$ vs c' for supercells of pure Fe, FeGa-A2, FeGa-A2 + $L6_0$, and FeGa-A2 + $2L6_0$. The slope of the line connecting the point for each supercell and the origin of coordinates corresponds to magnetostriction. Two enhancement effects are marked in the figure; effects 1 and 2 correspond to Ga solid-solution induced lattice softening and enhanced magnetoelastic coupling, respectively.

elastic constants, demonstrating that the introduction of $L6_0$ structure has weak effect on lattice stiffness.

The relations between magnetoelastic coefficient and elastic constants are indicated through plotting the location of each supercell in the $-\frac{1}{3}b_1$ versus c' two-dimensional coordinate system, as illustrated in Fig. 3(b). The slopes of the dashed lines, which connect the points of the corresponding supercell and the origin of coordinates, correspond to the magnetostriction, according to formulas (1) and (2). Herein, two enhancement effects are highlighted: (1) From pure Fe to FeGa-A2, the key factor of magnetostriction enhancement is the lattice softening caused by the Ga solid solution; the magnetoelastic coupling is only slightly reinforced. (2) From FeGa-A2 to $L6_0$ -inserted FeGa supercells, the elastic constant c' almost remains unchanged, while the magnetoelastic coupling effect is significantly strengthened as reflected by increase in $-\frac{1}{3}b_1$ by more than 2 times. Therefore, Ga alloying results in Ga solid solution and the formation of $L6_0$ nanoheterogeneity simultaneously; the former leads to the lattice softening and the latter one causes the strengthening in magnetoelastic coupling effect. The giant magnetostriction in the nanoheterogeneous Fe-Ga systems is expected to originate from the synergy of both lattice softening and magnetoelastic coupling enhancement effects.

The mechanism of each effect is, respectively, unveiled by first-principles calculations. It was already determined that the decrease in tetragonal shear modulus c' is attributed to the reduction in c_{11} . As we know, c_{11} reflects the ability of lattice to resist the deformation along the stress direction under a direct stress. Therefore, the strength of the bonds is considered as the key factor that dominates c_{11} . In order to find the mechanism where Ga solid solution induces the lattice softening, we utilized the electron localization function (ELF) to study the influence of solid-solution Ga on the chemical bonding, as shown in Fig. 4. ELF can display the localization degree of electron in a three-dimensional real space; thus, it is substantially adopted for investigating various chemical bonds, chemical reactions, organics, etc. Herein, in addition to the supercells of pure Fe and FeGa-A2, a bcc supercell

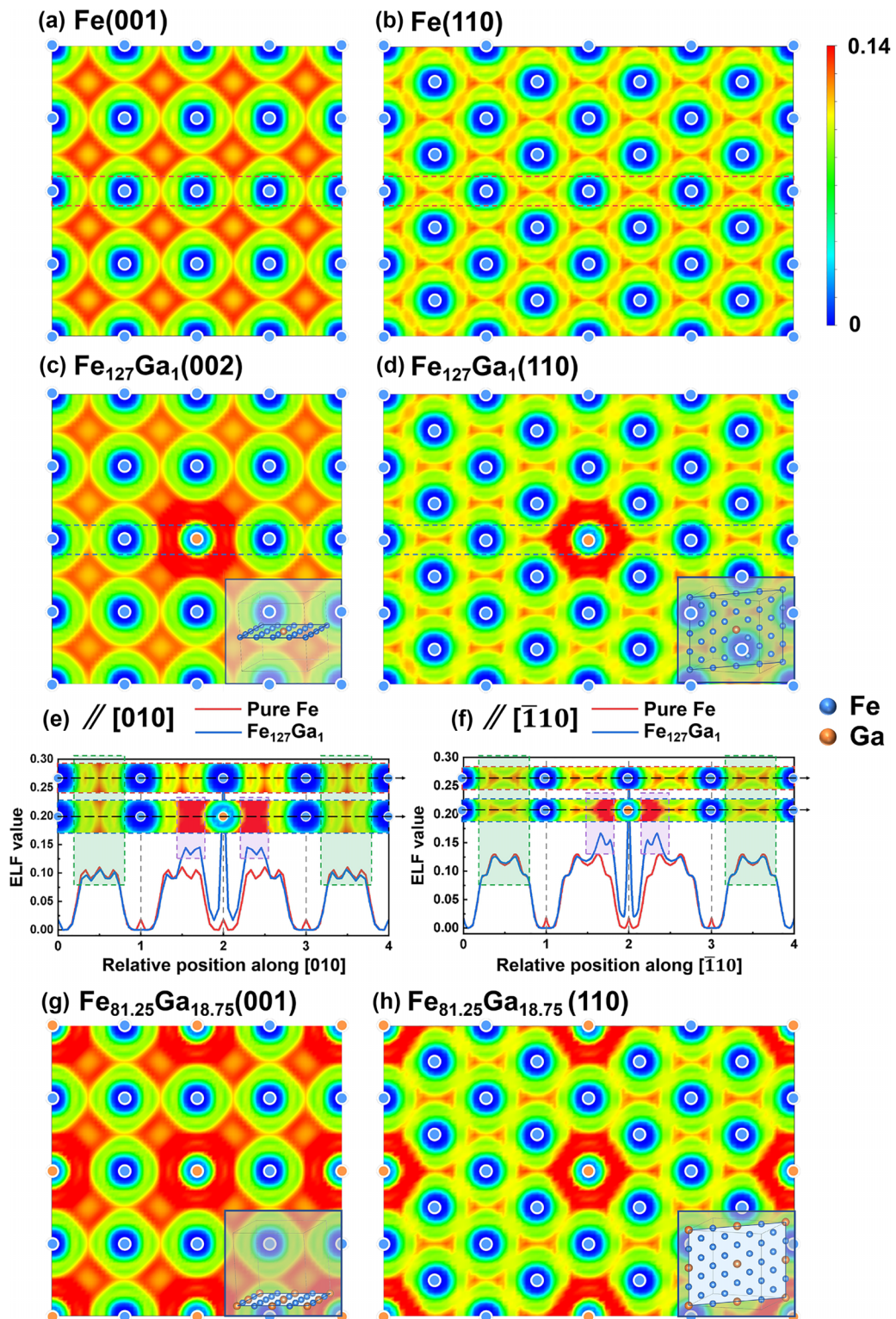


FIG. 4. (a), (b) ELF 2D profiles of pure Fe supercell viewing from (a) (001) plane and (b) (110) plane, respectively. (c), (d) ELF 2D profiles of $\text{Fe}_{127}\text{Ga}_1$ supercell viewing from (c) (002) plane and (d) (110) plane, respectively. (e), (f) Comparison in linear profiles of ELF values between pure-Fe and $\text{Fe}_{127}\text{Ga}_1$ supercells along (e) [001] and (f) [110] directions; the local 2D profiles of both lattices are also displayed for visual recognitions. (g), (h) ELF 2D profiles of FeGa-A2 supercell viewing from (a) (001) plane and (b) (110) plane, respectively.

which consists of 127 Fe atoms and 1 Ga atom is established. In this case, the influence of Ga can be obviously illustrated by comparing the pure Fe supercell and $\text{Fe}_{127}\text{Ga}_1$ supercell, and the gap between pure Fe and FeGa-A2 supercells is expected

to be plugged. The two-dimensional (2D) ELF profiles in the (002) and (110) planes of each supercell are presented in Fig. 4. For pure Fe, the 2D ELF figures exhibit the feature of a shared-electron interaction but the number of shared electrons

is far less than 1, indicating the typical metallic bonds. In addition, the weak covalent bonds induced by d - d hybridization of Fe atoms can be also observed, as shown in Figs. 4(a) and 4(b). When 1 Ga atom is introduced into the supercell, significantly localized electrons are observed around the center between the Ga and its neighbor Fe atoms, manifesting the strong covalent bonds induced by p - d hybridization, as shown in Figs. 4(c) and 4(d). Meanwhile, the Fe-Fe bonding framework, which is formed by the primary metallic bonds and minor d - d covalent bonds, is weakened by Ga atom as demonstrated by the color contrast. For a better distinction, the linear profiles showing the evolutions in ELF value along [001] and [110] axes in pure Fe and Fe₁₂₇Ga₁ supercells, are shown in Figs. 4(e) and 4(f). Simultaneously, locally magnified 2D ELF figures along [001] and [110] axes are also extracted for a visual comparison, as seen in the insets of Figs. 4(e) and 4(f). According to the linear profiles of pure Fe supercell, delocalization of electrons is demonstrated by the periodically emerged high ELF values (in the center between adjacent Fe atoms) and low ELF values (around Fe atoms), indicating a homogeneous metallic bond framework consisting of itinerant electrons. When Ga atom enters the supercell, p - d hybridized covalent Fe-Ga bonds are generated, as demonstrated by the risen ELF values in the position between Ga and adjacent Fe but closer to Ga [marked by purple rectangles in Figs. 4(e) and 4(f)]. Evidence of weakened Fe-Fe bonding is presented by the color contrast of 2D ELF images and slightly lower ELF values of Fe₁₂₇Ga₁ supercell according to the linear profiles, as marked by the green rectangles. In terms of the FeGa-A2 supercell (Fe_{81.25}Ga_{18.75}), more Ga atoms further decrease the strength of Fe-Fe bonding framework, as shown in Figs. 4(g) and 4(h). Therefore, it can be speculated that the sharp reduction in c_{11} is derived from the weakening of Fe-Fe bonds, which is induced by the solid solution of Ga.

The reinforcement in magnetoelastic coupling induced by the $L6_0$ structure is found by the analysis of density of states (DOS), using formulas (1) and (2) as the principle. Electronic structures of Fe atoms under different conditions are compared by based on the partial DOS (PDOS) results (corresponding to each 3d orbit), as shown in Fig. 5. It has been reported that in the limiting case of strong exchange splitting, the spin-up band is almost fully occupied. For a proper approximation, the entire empty states can be deemed to belong to spin-down bands, and the effect of the empty spin-up states is neglected. Therefore, only the coupling between spin-down states, especially the separation between the unoccupied-state energy (ϵ_u) and occupied-state energy (ϵ_o), should be taken into consideration for estimating the SOC energy. To simplify the analysis, we treated the d -band center energies of the unoccupied state and occupied state in the spin-down band as ϵ_u and ϵ_o , respectively, according to the formulas (4) and (5):

$$\epsilon_u = \frac{\int_0^\infty n_u(\epsilon)\epsilon d\epsilon}{\int_0^\infty n_u(\epsilon) d\epsilon}, \quad (4)$$

$$\epsilon_o = \frac{\int_{-\infty}^0 n_o(\epsilon)\epsilon d\epsilon}{\int_{-\infty}^0 n_o(\epsilon) d\epsilon}. \quad (5)$$

The areas of unoccupied and occupied states are colored red and blue, respectively. In the following, we studied the influence of $L6_0$ structure on SOC from “intrinsic” and

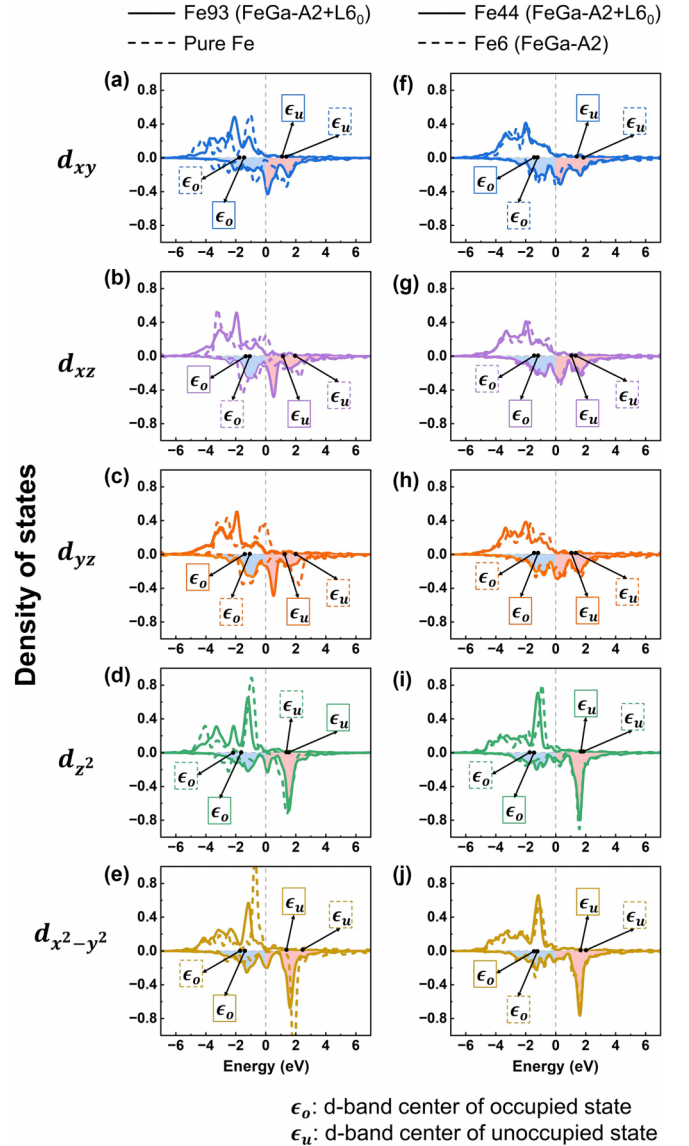


FIG. 5. (a)–(e) The comparison in partial density of states of Fe-93 in FeGa-A2 + $L6_0$ supercell and Fe atom in pure-Fe supercell, in order to show the intrinsic enhancement of SOC. (f)–(j) The comparison in partial density of states of Fe-44 in FeGa-A2 + $L6_0$ supercell and Fe-6 in FeGa-A2 supercell, in order to show the external enhancement of SOC.

“external” aspects, respectively. First, we compare the electronic structures of Fe-93 in FeGa-A2 + $L6_0$ supercell (Fe-93 is body-centered atom of local $L6_0$ structure in FeGa-A2 + $L6_0$ supercell) and Fe atom in pure Fe supercell, for demonstrating the intrinsic function of $L6_0$ structure on SOC, as shown in Figs. 5(a)–5(e). In the pure Fe, the feature of spin splitting is observed for each 3d orbit. Moreover, the Fermi level lies at the dip of the spin-down PDOS curve, indicating the high stability and symmetry of pure Fe supercell. Regarding Fe-93, the peaks in spin-down curves display a significant shift compared with those for pure Fe; this results in two new features: (1) Fermi level lies at the peak or the mountainside in spin-down PDOS curves, indicating the reduced stability of the $L6_0$ structure. This metastable nature may output local

TABLE I. Calculated elastic constants of Fe and FeGa alloys (unit: GPa).

Composition	Phase	c_{11} (GPa)	c_{12} (GPa)	c' (GPa)	c_{44} (GPa)	$-b_1$ (MPa)	λ_{001} (ppm)
Fe	A2	247.8	150.1	48.8	97.0	5.1	34.7
	A2	180.3	151.3	14.5	122.7	8.7	198.9
	A2 + $L6_0$	204.0	155.9	24.1	121.3	19.2	266.1
FeGa	A2 + $2L6_0$	197.6	157.0	20.3	118.6	18.8	307.9

elastic strain under external field, resulting in enhancement in magnetostriction enhancement. (2) The d -band center energy differences between the unoccupied and occupied states in the spin-down channel is remarkably lowered, as directly observed by the calculated values of ϵ_u and ϵ_o in Table I. As mentioned above, the $\epsilon_u - \epsilon_o$ dominates the strength of SOC interactions, which plays the key role in magnetostriction. For every $3d$ orbit, values of $\epsilon_u - \epsilon_o$ are dramatically lower for Fe-93 than pure Fe, leading to the strengthening in E^{SOC} . Therefore, the locally ordered $L6_0$ possesses a significant enhancement effect on magnetoelastic coupling; this can be deemed as an intrinsic function for improving magnetostriction.

Second, the electronic structures of Fe atoms in A2 matrix region in FeGa-A2 + $L6_0$ supercell (Fe-44) and FeGa-A2 supercell (Fe-6) are contrasted, in order to show the external effect of $L6_0$ structure on the SOC in the surrounding Fe atoms, as shown by PDOS results in Figs. 5(f)–5(j). The PDOS curves of each $3d$ orbit exhibit a similar landscape between Fe-44 and Fe-6, respectively, indicating their analogical atomic environments in the A2 matrix. The refined observation on the PDOS results manifests that for d_{xz} , d_{yz} , and d_{z^2} orbits, both ϵ_u and ϵ_o approach the Fermi level for Fe-44 simultaneously, resulting in lower values in $\epsilon_u - \epsilon_o$. In terms of $d_{x^2-y^2}$ and d_{xy} orbits, both ϵ_u and ϵ_o move to lower energy for Fe-44, while the decline of ϵ_u is more dramatic, leading to the decrease in the values of $\epsilon_u - \epsilon_o$ likewise. Therefore, the introduction of $L6_0$ structure leads to the reduction in values of $\epsilon_u - \epsilon_o$ for the Fe atom in A2 matrix (see Table II); this also strengthens SOC interaction externally, which also benefits magnetostriction. In a brief summary, the $L6_0$ structure simultaneously presents intrinsic (for Fe atoms which belong to $L6_0$ structures) and externally (for Fe atoms in the A2 matrix

around $L6_0$ structures) enhancement in SOC interactions, as demonstrated by the DOS results. These synergetic effects offer the probability to realize superior magnetostriction in $L6_0$ -contained FeGa alloys.

C. Occupation preference of alloyed atoms

Although $L6_0$ structure significantly benefits magnetostriction, its concentration in real FeGa alloys is limited due to its unstable nature according to our previous studies. However, further enhancement in magnetostriction is still promising to be achieved by the aforementioned two effects: lattice softening, and strengthening magnetoelastic coupling. Therefore, alloying the third element is a hopeful strategy, and the influence of different atoms on magnetostriction deserves to be systematically studied. We utilized FeGa-A2 + $2L6_0$ supercell as the basis, then selected four different atoms, including ferromagnetic $3d$ transition elements of Co and Ni, main-group element of P, and rare-earth element of Tb, to substitute every Fe atom. The ergodic energy difference of the alloyed supercell was compared with the original one, as shown in Fig. 6, for finding the occupation preference of different atoms. Additional structural relaxations were performed in these elementally doped FeGa supercells. The parameter setting of the relaxation is consistent with the previous calculation of the FeGa-based supercells, with the force convergence set to 10^{-3} eV/Å, and the energy convergence set to 10^{-6} eV per cell, respectively. The x axis corresponds to the numerical order of Fe atoms in the original FeGa-A2 + $2L6_0$ supercell, as illustrated in Fig. 1(d). For each type of alloyed atom, two featured substitution positions are extracted: the highest-energy difference position (HEP) and lowest-energy difference position (LEP), as colored brown and red in Fig. 6, respectively.

TABLE II. ϵ_o , ϵ_u and $\epsilon_o - \epsilon_u$ of several selected Fe atoms in Fe and FeGa supercells (unit: eV).

Atom	Parameter	d_{xy}	d_{xz}	d_{yz}	d_{z^2}	$d_{x^2-y^2}$
Pure Fe	ϵ_o	-1.81	-1.23	-1.14	-2.09	-1.81
	ϵ_u	1.47	2.06	2.17	1.48	2.30
	$\epsilon_o - \epsilon_u$	3.28	3.29	3.31	3.57	4.11
Fe-93 (FeGa-A2 + $L6_0$)	ϵ_o	-1.51	-1.54	-1.55	-1.62	-1.50
	ϵ_u	1.26	1.42	1.43	1.58	1.66
	$\epsilon_o - \epsilon_u$	2.77	2.96	2.98	3.20	3.16
Fe-44 (FeGa-A2 + $L6_0$)	ϵ_o	-1.45	-1.45	-1.44	-1.64	-1.60
	ϵ_u	1.40	1.42	1.44	1.65	1.68
	$\epsilon_o - \epsilon_u$	2.85	2.87	2.88	3.29	3.28
Fe-6 (FeGa-A2)	ϵ_o	-1.37	-1.51	-1.52	-1.84	-1.56
	ϵ_u	1.86	1.62	1.67	1.69	1.80
	$\epsilon_o - \epsilon_u$	3.23	3.13	3.19	3.53	3.36

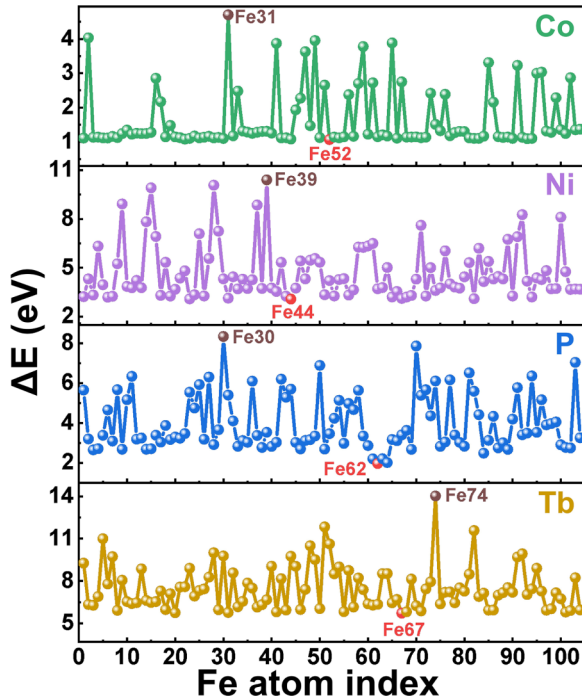


FIG. 6. The ergodic energy difference of the alloyed supercells compared with the original FeGa-A2 + 2L₆₀ supercell: (a) Co substitution; (b) Ni substitution; (c) P substitution; and (d) Tb-substitution.

The atomic environment, including the nearest- and next-nearest atoms of each doped atom at the HEP and LEP, is extracted for a better visualization, as shown in Figs. 7(a)–7(h). LEPs of Co and Ni correspond to Fe-52 (body center of L₆₀-1) and Fe-44 (body center of L₆₀-2), respectively, indicating that both Co and Ni prefer to occupy the body center of L₆₀ structure. The HEPs of Co and Ni also include 4 Ga atoms in the surrounding, but the spatial configuration is different. Therefore, Co and Ni present the occupation preference of selection in the surrounding Ga atom distributions. In terms of P, it prefers to occupy Fe-62 position of which the nearest- and next-nearest atoms are all Fe atoms, while P is unfavorable to occupy the position with considerable Ga atoms around (Fe-30), as shown in Fig. 7(f). In contrast to P, Tb tends to occupy the position with 4 nearest Ga atoms (Fe-67), but is not inclined to occupy the position of which the nearest- and next-nearest atoms are Fe (Fe-74).

D. Elastic and magnetostrictive properties of alloyed FeGa solid solutions

We calculated the elastic constant, magnetoelastic coupling coefficient, and magnetostriction of the alloyed supercells with lowest energy differences (namely as FeGa-Ni, FeGa-Co, FeGa-P, and FeGa-Tb, respectively); the results of original FeGa-A2 + 2L₆₀ supercell are also listed for comparison, which are marked as dashed lines in Fig. 8. The dopant of Co slightly decreases magnetostriction from 308 to 298 ppm, which is caused by the faint weakening in magnetoelastic coupling effect. Ni tends to occupy similar position compared with Co; nevertheless, magnetostriction displays a sharper reduction to 229 ppm than that of Co doping; this should be

mainly attributed to the increase in c' . Regarding P doping, although P can induce the lattice softening (lower c') in FeGa supercell, however the magnetoelastic coupling coefficient is almost reduced by half. The dominant action of the latter effect leads to a degraded magnetostriction of 207 ppm in P-doped FeGa alloy. For the rare-earth element Tb, c' is mildly decreased, manifesting the lattice-softening effect induced by Tb. More importantly, the magnetoelastic coupling is remarkably strengthened as reflected by the rise in $-b_1$ by 45%; thus, the magnetostriction is enhanced to 738 ppm.

In the following, we individually investigate the mechanism of how doping the third atom affects magnetostriction of FeGa alloy. Due to the high similarities in occupation preference, electronic structure, and atomic magnetism between Co and Ni, we selected Ni for discussion. It is already inferred from Fig. 8 that the substitution of the body-centered Fe atom in L₆₀ structure by Ni mainly leads to the lattice hardening. Therefore, the 2D ELF profiles of undoped and Ni-doped supercells are compared to reveal the influence of Ni doping on the bond framework, as shown in Fig. 9. By viewing the ELF profiles in (001) plane, it can be found that the basic metallic-bond framework is maintained by Ni doping, since Ni only has 2 more 3d valence electrons than Fe. From the color contrast, the metallic bonds around the Ni atom are demonstrated to be enhanced, as marked by the white circles in Figs. 8(a) and 8(c). When viewing from the $(\bar{1}01)$ plane, Ga–Ga and Fe–Ga bonds along [100] axes are observed to be simultaneously reinforced by Ni doping, which is demonstrated by the higher ELF values in Figs. 9(b) and 9(d). For a more distinct view, the linear profiles showing the evolutions in ELF value along [100] and [101] axes in FeGa-A2 + 2L₆₀ and FeGa-Ni supercells are shown in Figs. 9(e) and 9(f). Simultaneously, locally magnified 2D ELF figures along the two axes are also extracted for a visual comparison, as seen in the insets of Figs. 9(e) and 9(f). According to the linear profiles, obviously higher ELF values (red curves) can be observed in FeGa-Ni supercell, indicating stronger metallic bonds. Therefore, the substitution of Fe by Ni in the body center of L₆₀ causes the reinforcement of the metallic-bond framework; this results in the increase in c' , degrading magnetostriction.

The degradation in magnetostriction for P-doped FeGa supercell, as well as the increase in magnetostriction for Tb-doped FeGa supercell, should originate from the weakening or enhancement in magnetoelastic coupling effect. Therefore, Fe atoms adjacent to the LEP of P-doped supercell (Fe-29) and adjacent to the LEP of Tb-doped supercell (Fe-35) are investigated by comparing the ϵ_u and ϵ_o parameters at undoped and P-doped situations, as shown in Fig. 10. The corresponding PDOS profiles are displayed in Figs. S1 and S2 (see Supplemental Material [68]). For P-doped supercells, the equivalent 3d orbitals including d_{xy} , d_{xz} , and d_{yz} , both ϵ_u and ϵ_o shift away from E_F , leading to the significant increase in values of $\epsilon_u - \epsilon_o$, as shown in Fig. 10(a). In contrast, ϵ_u and ϵ_o simultaneously shift to higher values for $d_{x^2-y^2}$ and d_{z^2} orbitals induced by P doping. Therefore, the corresponding values of $\epsilon_u - \epsilon_o$ of these two orbitals are slightly decreased, as displayed in Fig. 10(a). By combining the contribution of each orbital, the magnetoelastic coupling effect is concluded to be impaired. In addition, P atom has valence electrons of $3s^2 3p^3$, so P normally bonds by using the $s-p$ hybrid orbitals to generate

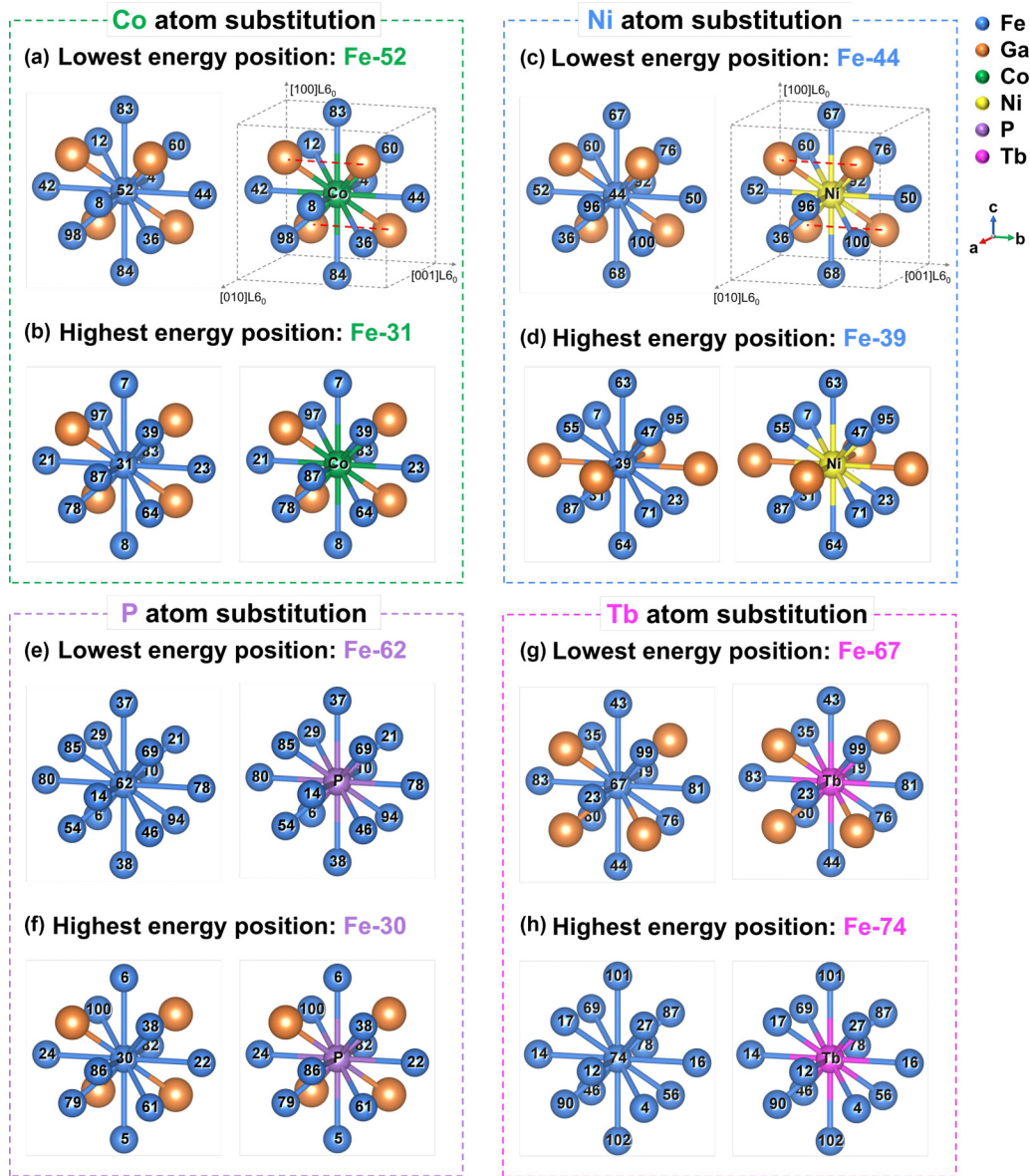


FIG. 7. The atomic environments of alloyed atom at the corresponding lowest-energy positions (LEPs) and highest-energy positions (HEPs): (a) LEP of Co substitution; (b) HEP of Co substitution; (c) LEP of Ni substitution; (d) HEP of Ni substitution; (e) LEP of P substitution; (f) HEP of P substitution; (g) LEP of Tb substitution; and (h) HEP of Tb substitution.

covalent bond. In this case, P atom does not have unpaired electrons so that magnetoelastic coupling effect is absent. Therefore, the substitution of Fe by P weakens the magnetoelastic coupling effect not only in the Fe atoms around P, but also by decreasing the concentration of ferromagnetic Fe atoms; therefore, magnetostriction is significantly degraded.

Among the four selected atoms, heavy rare-earth Tb is the sole element which is found to significantly enhance magnetostriction [69]; the dominant factor is the enhancement in SOC effect. On one side, Tb atom presents strong SOC effect on account of valence electronic structure of $4f^9$, resulting in a giant magnetostriction of ~ 5000 ppm in pure Tb. Here, we focus on the influence of Tb on the SOC effect in the surrounding Fe atoms (Fe-35 is selected as a

typical example), as presented in Fig. 10(b) and Fig. S2 (see Supplemental Material [68]). Overall, doping Tb atom leads to the decrease in $\epsilon_u - \epsilon_o$ for every orbit, enhancing magnetoelastic coupling effect as well as magnetostriction, as presented in Fig. 10(b). Moreover, the values of $\epsilon_u - \epsilon_o$ fall much more sharply in $d_{x^2-y^2}$ and d_{z^2} than those in d_{xy} , d_{xz} and d_{yz} . In detail, for the three equivalent $3d$ orbitals of d_{xy} , d_{xz} , and d_{yz} , the spin-down DOS curves shift left overall. Accompanying that, the difference between d -band centers of unoccupied state ϵ_u and occupied ϵ_o slightly decreases, as calculated in Table S1 (see Supplemental Material [68]). Regarding the left two equivalent $3d$ orbitals of $d_{x^2-y^2}$ and d_{z^2} , the left shift of unoccupied states and right shift of occupied states are simultaneously detected, resulting in a sharp reduction in the values of $\epsilon_u - \epsilon_o$. Therefore,

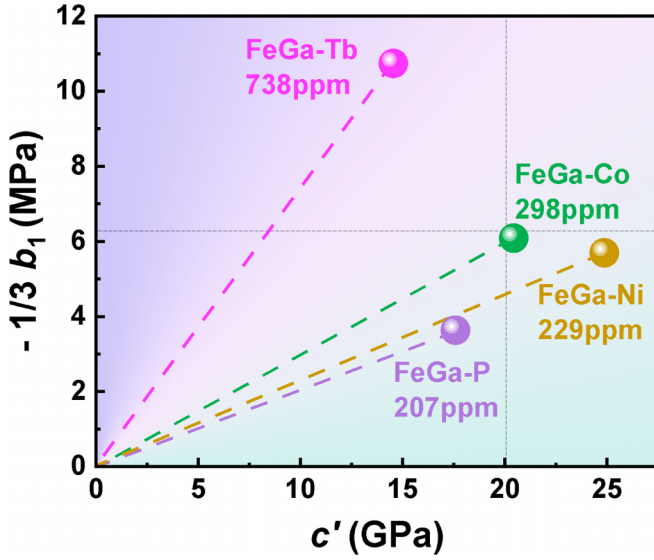


FIG. 8. Calculated magnetoelastic coupling coefficient, elastic constant of c' , and magnetostriction of FeGa-Co, FeGa-Ni, FeGa-P, and FeGa-Tb supercells. The gray dashed lines correspond to the levels of $-\frac{1}{3}b_1$ and c' of original FeGa-A2 + 2L60 supercell.

doping the heavy rare-earth Tb atom induces substantial enhancement in SOC effect for the surrounding Fe atoms, which is responsible for the reinforced magnetoelastic coupling as well as magnetostriction.

Figure 11 summarizes the measured elastic constant (c') and magnetoelastic coupling coefficient ($-b_1$) of already-emerged Fe-based magnetostrictive materials, including FeGa, FeAl, FeGe, FeSi, FeGaAl, FeGaGe, etc. The detailed data are listed in Table S2 (see Supplemental Material [68]). The calculated results in this work are also presented for comparison. Pure Fe presents significantly greater lattice stiffness and quite weak magnetoelastic coupling. By alloying the main-group elements of Ga, Al, Si, or Ge, c' can be significantly decreased, while $-b_1$ exhibits peaks with the variation in the solid-solution content of each element. Alloying Al and Ga to pure Fe can remarkably strengthen the magnetoelastic coupling effect, while alloy Si or Ge fail to achieve that. Among these Fe-based solid solutions, FeGa alloys exhibit superior magnetostriction, on account of the remarkably higher $-b_1$. It deserves to be noted that the experimentally measured c' and $-b_1$ are in good agreement with our computed results, indicating the reliability of the calculation methods. Compared with the existing Fe-based solid solutions, the established FeGa supercells (A2, A2 + L60, A2 + 2L60) and alloyed FeGa supercells (FeGa-Ni, FeGaCo, FeGa-P) do not show obvious advantages in c' and $-b_1$. The FeGa-Tb supercell presents substantially superior $-b_1$ as well as magnetostriction. Therefore, FeGa magnetostrictive materials with the solid solution are promising to show superior performance, which is partially demonstrated by our previous work. The problem which still needs to be addressed is the near-zero solid solubility of Tb in FeGa A2 matrix; the fabrication of (001) textured polycrystalline or single-crystal FeGa-Tb alloys under a rapid cooling rate remains a challenge in the aspects of developing new apparatus as well as technologies.

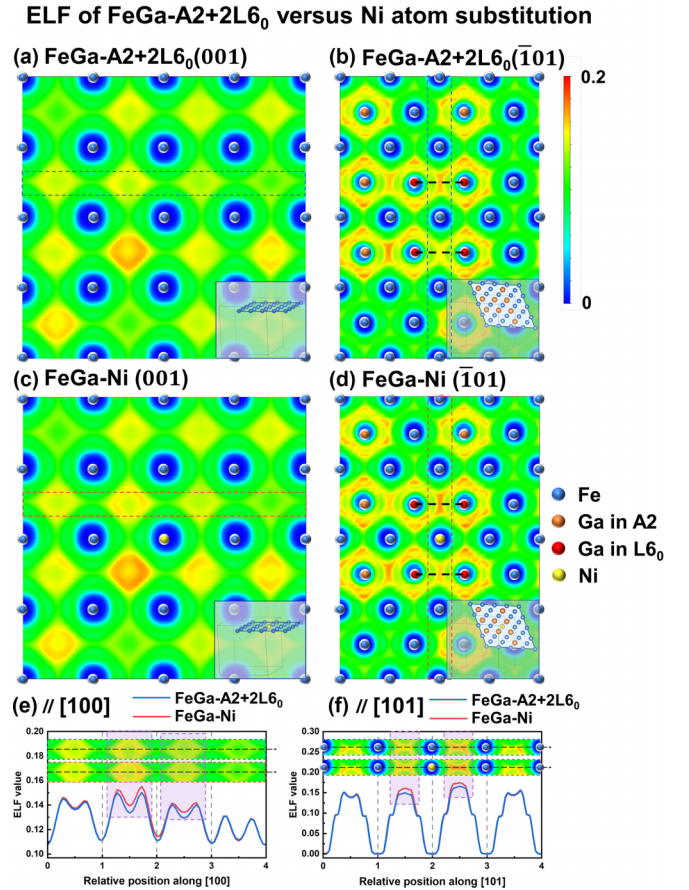


FIG. 9. (a), (b) ELF 2D profiles of FeGa-A2 + 2L60 supercell viewing from (a) (001) plane and (b) $(\bar{1}01)$ plane, respectively. (c), (d) ELF 2D profiles of FeGa-Ni supercell viewing from (c) (001) plane and (d) $(\bar{1}01)$ plane, respectively. (e), (f) Comparison in linear profiles of ELF values between FeGa-A2 + 2L60 supercell and FeGa-Ni supercell along (e) [100] and (f) [101] directions; the local 2D profiles of both supercells are also displayed for visual recognitions. (g), (h) ELF 2D profiles of FeGa-A2 + 2L60 supercell viewing from (a) (001) plane and (b) $(\bar{1}01)$ plane, respectively.

IV. CONCLUSION

(1) The giant magnetostriction in FeGa magnetostrictive alloys is demonstrated to originate from two synergetic effects: lattice softening and strengthened magnetoelastic coupling effect, as reflected by the reduced elastic constant c' and increased magnetoelastic coupling coefficient $|b_1|$, respectively. The former effect is induced by the random solid solution of Ga atoms in the bcc-A2 Fe supercell, because Ga atoms can induce the weakening of the Fe-Fe metallic bonds in the nearest- and second-nearest Fe atom framework, leading to significant decrease in c_{11} and thus lower c' . The latter effect is caused by the locally ordered L60 structure in A2-FeGa supercell. L60 structure concurrently has intrinsically SOC-strengthened Fe atoms, and can induce external reinforcement in SOC effect for the surrounding Fe atoms; this results in stronger magnetoelastic coupling and further improves magnetostriction.

(2) The occupation preferences of various doped atoms and the correlated evolution in magnetostriction and the

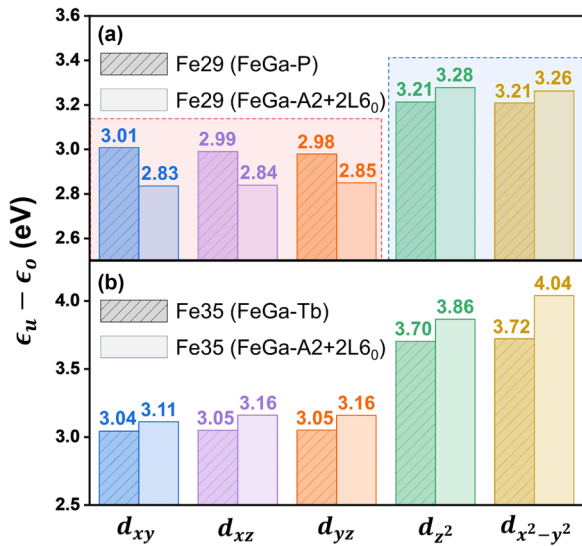


FIG. 10. Comparison in values of $\epsilon_u - \epsilon_o$ of each 3d orbit for the selected Fe atoms in the case of undoping and doping. (a) Fe29 in the case of P doping. (b) Fe35 in the case of Tb doping.

mechanism are revealed. The ferromagnetic 3d transition atoms Co and Ni tend to occupy the body center of locally ordered $L6_0$ structure, leading to the lattice hardening. The resultant increase in c' reduces magnetostriction in Co-doped or Ni-doped FeGa alloys. The main-group element P tend to generate strong $p-d$ covalent bonds with Fe; therefore, P atom tends to substitute the atomic site with the nearest- and second-nearest sites with all Fe atoms. P doping weakens the SOC and magnetoelastic coupling, leading to degradation in magnetostriction. Rare-earth element Tb can induce a significant enhancement in SOC; the magnetoelastic coupling coefficient can be improved by approximately double, resulting in significantly improved magnetostriction from 308 to 738 ppm.

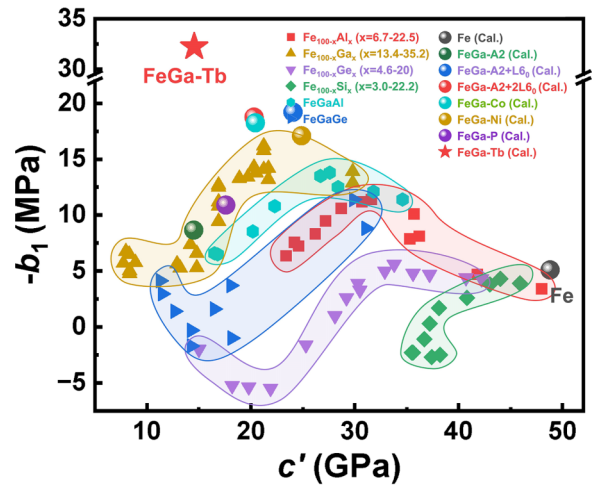


FIG. 11. Summary of experimentally measured c' and $-b_1$ of various Fe-based solid solutions (extracted from literature) [19,24,28,31,35] and the theoretically computed results of the FeGa-based supercells in this work.

(3) This work offers an in-depth and systematic understanding of the origin of giant magnetostriction in FeGa alloys, and also specifies the concept for designing high-performance FeGa-based magnetostrictive materials through alloys traces of third elements. These may shed light on future developments in the theory and fabrication of magnetostrictive materials.

ACKNOWLEDGMENTS

This work was supported by the National Key R&D Program of China under Grant No. 2023YFB3508700), the National Natural Science Foundation of China (NSFC) under Grants No. 52121001, No. 52227801, No. 52271162, and No. 52250313, and the Fundamental Research Funds for the Central Universities.

[1] A. E. Clark, *Ferromagnetic Materials* (North-Holland, Amsterdam, 1980).

[2] J. M. D. Coey, *Magnetism and Magnetic Materials* (Cambridge University Press, Cambridge, 2009).

[3] J. Atulasimha and A. B. Flatau, A review of magnetostrictive iron-gallium alloys, *Smart Mater. Struct.* **20**, 43001 (2011).

[4] A. G. Olabi and A. Grunwald, Design and application of magnetostrictive materials, *Mater. Des.* **29**, 469 (2008).

[5] J. Atulasimha, A. B. Flatau, and E. Summers, Characterization and energy-based model of the magnetomechanical behavior of polycrystalline iron-gallium alloys, *Smart Mater. Struct.* **16**, 1265 (2007).

[6] E. Quandt and A. Ludwig, Magnetostrictive actuation in microsystems, *Sens. Actuators, A* **81**, 275 (2000).

[7] Z. Deng and M. J. Dapino, Review of magnetostrictive vibration energy harvesters, *Smart Mater. Struct.* **26**, 103001 (2017).

[8] H. Hou, P. Finkel, M. Staruch, J. Cui, and I. Takeuchi, Ultra-low-field magneto-elastocaloric cooling in a multiferroic composite device, *Nat. Commun.* **9**, 4075 (2018).

[9] F. Narita and M. Fox, A review on piezoelectric, magnetostrictive, and magnetoelectric materials and device technologies for energy harvesting applications, *Adv. Eng. Mater.* **20**, 1700743 (2018).

[10] G. Wade, Human uses of ultrasound: Ancient and modern, *Ultrasonics* **38**, 1 (2000).

[11] N. Wang, Y. Liu, H. Zhang, X. Chen, and Y. Li, Fabrication, magnetostriction properties and applications of Tb-Dy-Fe alloys: A review, *China Foundry* **13**, 75 (2016).

[12] R. Abbundi and A. Clark, Anomalous thermal expansion and magnetostriction of single crystal Tb₂₇Dy₇₃Fe₂, *IEEE Trans. Magn.* **13**, 1519 (1977).

[13] G. Engdahl and I. D. Mayergoyz, *Handbook of Giant Magnetostrictive Materials* (Academic Press, San Diego, 2000).

[14] A. E. Clark, Magnetostrictive rare earth-Fe₂ compounds, in *Handbook of Ferromagnetic Materials* (Elsevier, New York, 1980), Vol. 1, pp. 531-589.

[15] A. E. Clark, R. Abbundi, H. T. Savage, and O. D. McMasters, Magnetostriction of rare earth-Fe₂ laves phase compounds, *Physica B+C (Amsterdam)* **86-88**, 73 (1977).

- [16] A. E. Clark and H. S. Belson, Giant room-temperature magnetostrictions in TbFe₂ and DyFe₂, *Phys. Rev. B* **5**, 3642 (1972).
- [17] J. D. Verhoeven, J. E. Ostenson, E. D. Gibson, and O. D. McMasters, The effect of composition and magnetic heat treatment on the magnetostriction of Tb_xDy_{1-x}Fe_y twinned single crystals, *J. Appl. Phys.* **66**, 772 (1989).
- [18] A. E. Clark, B. F. DeSavage, and R. Bozorth, Anomalous thermal expansion and magnetostriction of single-crystal dysprosium, *Phys. Rev.* **138**, A216 (1965).
- [19] A. E. Clark, J. B. Restorff, M. Wun-Fogle, T. A. Lograsso, and D. L. Schlager, Magnetostrictive properties of body-centered cubic Fe-Ga and Fe-Ga-Al alloys, *IEEE Trans. Magn.* **36**, 3238 (2000).
- [20] Y. He, C. Jiang, W. Wu, B. Wang, H. Duan, H. Wang, T. Zhang, J. Wang, J. Liu, Z. Zhang *et al.*, Giant heterogeneous magnetostriction in Fe-Ga alloys: Effect of trace element doping, *Acta Mater.* **109**, 177 (2016).
- [21] Y. He, X. Ke, C. Jiang, N. Miao, H. Wang, J. M. D. Coey, Y. Wang, and H. Xu, Interaction of trace rare-earth dopants and nanoheterogeneities induces giant magnetostriction in Fe-Ga alloys, *Adv. Funct. Mater.* **28**, 1800858 (2018).
- [22] Y. He, J. M. D. Coey, R. Schaefer, and C. Jiang, Determination of bulk domain structure and magnetization processes in bcc ferromagnetic alloys: Analysis of magnetostriction in Fe₈₃Ga₁₇, *Phys. Rev. Mater.* **2**, 014412 (2018).
- [23] T. Ma, J. Gou, S. Hu, X. Liu, C. Wu, S. Ren, H. Zhao, A. Xiao, C. Jiang, X. Ren *et al.*, Highly thermal-stable ferromagnetism by a natural composite, *Nat. Commun.* **8**, 13937 (2017).
- [24] J. B. Restorff, M. Wun-Fogle, K. B. Hathaway, A. E. Clark, T. A. Lograsso, and G. Petculescu, Tetragonal magnetostriction and magnetoelastic coupling in Fe-Al, Fe-Ga, Fe-Ge, Fe-Si, Fe-Ga-Al, and Fe-Ga-Ge alloys, *J. Appl. Phys.* **111**, 023905 (2012).
- [25] G. A. Marchant, C. E. Patrick, and J. B. Staunton, Ab initio calculations of temperature-dependent magnetostriction of Fe and A2 Fe_{1-x}Ga_x within the disordered local moment picture, *Phys. Rev. B* **99**, 054415 (2019).
- [26] K. Yan, Y. Xu, J. Niu, Y. Wu, Y. Li, B. Gault, S. Zhao, X. Wang, Y. Li, J. Wang, K. P. Skokov, O. Gutfleisch, H. Wu, D. Jiang, Y. He, and C. Jiang, Unraveling the origin of local chemical ordering in Fe-based solid-solutions, *Acta Mater.* **264**, 119583 (2024).
- [27] J. Cullen, A. Clark, M. Wun-Fogle, J. Restorff, and T. Lograsso, Magnetoelasticity of Fe-Ga and Fe-Al alloys, *J. Magn. Magn. Mater.* **226-230**, 948 (2001).
- [28] G. Petculescu, A. O. Mandru, W. M. Yuhasz, T. A. Lograsso, M. Wun-Fogle, J. B. Restorff, A. E. Clark, and K. B. Hathaway, The effect of partial substitution of Ge for Ga on the elastic and magnetoelastic properties of Fe-Ga alloys, *J. Appl. Phys.* **107**, 09A926 (2010).
- [29] Y. He, Y. Han, P. Stamenov, B. Kundys, J. M. D. Coey, C. Jiang, and H. Xu, Investigating non-Joulian magnetostriction, *Nature (London)* **556**, E5 (2018).
- [30] Y. Wu, Y. Chen, C. Meng, H. Wang, X. Ke, J. Wang, J. Liu, T. Zhang, R. Yu, J. M. D. Coey *et al.*, Multiscale influence of trace Tb addition on the magnetostriction and ductility of (100) oriented directionally solidified Fe-Ga crystals, *Phys. Rev. Mater.* **3**, 033401 (2019).
- [31] Y. J. Chen, Z. H. Fu, Y. Y. Wu, Y. C. Xu, Y. Xiao, J. M. Wang, R. F. Zhang, and C. B. Jiang, Giant heterogeneous magnetostriction induced by charge accumulation-mediated nanoinclusion formation in dual-phase nanostructured systems, *Acta Mater.* **213**, 116975 (2021).
- [32] H. Cao, F. Bai, J. Li, D. D. Viehland, T. A. Lograsso, and P. M. Gehring, Structural studies of decomposition in Fe-x at.%Ga alloys, *J. Alloy. Compd.* **465**, 244 (2008).
- [33] O. Ikeda, R. Kainuma, I. Ohnuma, K. Fukamichi, and K. Ishida, Phase equilibria and stability of ordered b.c.c. phases in the Fe-rich portion of the Fe-Ga system, *J. Alloy. Compd.* **347**, 198 (2002).
- [34] A. E. Clark, K. B. Hathaway, M. Wun-Fogle, J. B. Restorff, T. A. Lograsso, V. M. Keppens, G. Petculescu, and R. A. Taylor, Extraordinary magnetoelasticity and lattice softening in bcc Fe-Ga alloys, *J. Appl. Phys.* **93**, 8621 (2003).
- [35] G. Petculescu, K. B. Hathaway, T. A. Lograsso, M. Wun-Fogle, and A. E. Clark, Magnetic field dependence of galfenol elastic properties, *J. Appl. Phys.* **97**, 10M315 (2005).
- [36] H. Wang, Z. D. Zhang, R. Q. Wu, and L. Z. Sun, Large-scale first-principles determination of anisotropic mechanical properties of magnetostrictive Fe-Ga alloys, *Acta Mater.* **61**, 2919 (2013).
- [37] M. Wuttig, L. Dai, and J. Cullen, Elasticity and magnetoelasticity of Fe-Ga solid solutions, *Appl. Phys. Lett.* **80**, 1135 (2002).
- [38] S. Bhattacharyya, J. R. Jinschek, A. Khachaturyan, H. Cao, J. F. Li, and D. Viehland, Nanodispersed DO3-phase nanostructures observed in magnetostrictive Fe-19% Ga Galfenol alloys, *Phys. Rev. B* **77**, 104107 (2008).
- [39] H. Cao, P. M. Gehring, C. P. Devreugd, J. A. Rodriguez-Rivera, J. Li, and D. Viehland, Role of nanoscale precipitates on the enhanced magnetostriction of heat-treated galfenol (Fe_{1-x}Ga_x) alloys, *Phys. Rev. Lett.* **102**, 127201 (2009).
- [40] J. Gou, T. Yang, R. Qiao, Y. Liu, and T. Ma, Formation mechanism of tetragonal nanoprecipitates in Fe-Ga alloys that dominate the material's large magnetostriction, *Scr. Mater.* **185**, 129 (2020).
- [41] M. Laver, C. Mudivarthi, J. R. Cullen, A. B. Flatau, W.-C. Chen, S. M. Watson, and M. Wuttig, Magnetostriction and magnetic heterogeneities in iron-gallium, *Phys. Rev. Lett.* **105**, 027202 (2010).
- [42] M. P. Ruffoni, S. Pascarelli, R. Grössinger, R. S. Turtelli, C. Bormio-Nunes, and R. F. Pettifer, Direct measurement of intrinsic atomic scale magnetostriction, *Phys. Rev. Lett.* **101**, 147202 (2008).
- [43] S. Wei, L. G. Ferreira, J. E. Bernard, and A. Zunger, Electronic properties of random alloys: Special quasirandom structures, *Phys. Rev. B* **42**, 9622 (1990).
- [44] A. Zunger, S.-H. Wei, L. G. Ferreira, and J. E. Bernard, Special quasirandom structures, *Phys. Rev. Lett.* **65**, 353 (1990).
- [45] X. Chen, Q. Wang, Z. Cheng, M. Zhu, H. Zhou, P. Jiang, L. Zhou, Q. Xue, F. Yuan, J. Zhu *et al.*, Direct observation of chemical short-range order in a medium-entropy alloy, *Nature (London)* **592**, 712 (2021).
- [46] Z. Lei, X. Liu, Y. Wu, H. Wang, S. Jiang, S. Wang, X. Hui, Y. Wu, B. Gault, P. Kontis *et al.*, Enhanced strength and ductility in a high-entropy alloy via ordered oxygen complexes, *Nature (London)* **563**, 546 (2018).
- [47] C. Niu, C. R. LaRosa, J. Miao, M. J. Mills, and M. Ghazisaeidi, Magnetically-driven phase transformation strengthening in high entropy alloys, *Nat. Commun.* **9**, 1363 (2018).
- [48] C. Kittel, Physical theory of ferromagnetic domains, *Rev. Mod. Phys.* **21**, 541 (1949).

- [49] R. Wu and A. J. Freeman, Spin-orbit induced magnetic phenomena in bulk metals, and their surfaces, and interfaces, *J. Magn. Mater.* **200**, 498 (1999).
- [50] R. Q. Wu, L. J. Chen, A. Shick, and A. J. Freeman, First-principles determinations of magneto-crystalline anisotropy and magnetostriction in bulk and thin-film transition metals, *J. Magn. Mater.* **177–181**, 1216 (1998).
- [51] J. R. Cullen, A. E. Clark, and K. B. Hathaway, in *Materials Science and Technology*, edited by R. W. Cahn, P. Haasen, and E. J. Kramer (John Wiley & Sons, Hoboken, NJ, 2006).
- [52] L. Berger, Evidence for split bands in Ni-Fe from specific heat, g-factor, and magnetostriction data, *Physica B+C* **91**, 31 (1977).
- [53] H. Wang, Y. N. Zhang, T. Yang, Z. D. Zhang, L. Z. Sun, and R. Q. Wu, Ab initio studies of the effect of nanoclusters on magnetostriction of $\text{Fe}_{1-x}\text{Ga}_x$ alloys, *Appl. Phys. Lett.* **97**, 262505 (2010).
- [54] Y. N. Zhang, J. X. Cao, and R. Q. Wu, Rigid band model for prediction of magnetostriction of iron-gallium alloys, *Appl. Phys. Lett.* **96**, 062508 (2010).
- [55] F. Mahfouzi, G. P. Carman, and N. Kioussis, Magnetoelastic and magnetostrictive properties of Co_2XAl Heusler compounds, *Phys. Rev. B* **102**, 094401 (2020).
- [56] G. A. Marchant, C. D. Woodgate, C. E. Patrick, and J. B. Staunton, Ab initio calculations of the phase behavior and subsequent magnetostriction of $\text{Fe}_{1-x}\text{Ga}_x$ within the disordered local moment picture, *Phys. Rev. B* **103**, 094414 (2021).
- [57] H. Wang and R. Wu, First-principles investigation of the effect of substitution and surface adsorption on the magnetostrictive performance of Fe-Ga alloys, *Phys. Rev. B* **99**, 205125 (2019).
- [58] A. van de Walle, P. Tiwary, M. de Jong, D. L. Olmsted, M. Asta, A. Dick, D. Shin, Y. Wang, L. Chen, and Z. Liu, Efficient stochastic generation of special quasirandom structures, *Calphad* **42**, 13 (2013).
- [59] G. Kresse and J. Furthmüller, Efficient iterative schemes for ab initio total-energy calculations using a plane-wave basis set, *Phys. Rev. B* **54**, 11169 (1996).
- [60] P. E. Blöchl, Projector augmented-wave method, *Phys. Rev. B* **50**, 17953 (1994).
- [61] J. P. Perdew, K. Burke, and M. Ernzerhof, Generalized gradient approximation made simple, *Phys. Rev. Lett.* **77**, 3865 (1996).
- [62] P. Nieves, S. Arapan, S. H. Zhang, A. P. Kądziaława, R. F. Zhang, and D. Legut, MAELAS: MAGneto-ELAStic properties calculation via computational high-throughput approach, *Comput. Phys. Commun.* **264**, 107964 (2021).
- [63] P. Nieves, S. Arapan, S. H. Zhang, A. P. Kądziaława, R. F. Zhang, and D. Legut, MAELAS 2.0: A new version of a computer program for the calculation of magneto-elastic properties, *Comput. Phys. Commun.* **271**, 108197 (2022).
- [64] S. H. Zhang and R. F. Zhang, AELAS: Automatic ELAStic property derivations via high-throughput first-principles computation, *Comput. Phys. Commun.* **220**, 403 (2017).
- [65] J. Hu and R. Wu, Control of the magnetism and magnetic anisotropy of a single-molecule magnet with an electric field, *Phys. Rev. Lett.* **110**, 097202 (2013).
- [66] D. Wang, R. Wu, and A. J. Freeman, State-tracking first-principles determination of magnetocrystalline anisotropy, *Phys. Rev. Lett.* **70**, 869 (1993).
- [67] V. Wang, N. Xu, J.-C. Liu, G. Tang, and W.-T. Geng, VASPKIT: A user-friendly interface facilitating high-throughput computing and analysis using VASP code, *Comput. Phys. Commun.* **267**, 108033 (2021).
- [68] See Supplemental Material at <http://link.aps.org/supplemental/10.1103/PhysRevB.109.014417> for the PDOS profiles of alloyed FeGa supercells and elastic constants (c') and magneto-elastic coupling coefficient (b_1) of various Fe-based solid solutions.
- [69] C. Meng, Y. Wu, and C. Jiang, Design of high ductility FeGa magnetostrictive alloys: Tb doping and directional solidification, *Mater. Des.* **130**, 183 (2017).